Earth Observation Data Analysis - Homework 03

Gioia Mancini, Christian Brignone

August 31, 2020

In this homework three different problems are addressed:

- Earthquake detection by SAR differential interferometry
- Ship detection by SAR backscattering
- Flood detection by SAR backscattering

Earthquake detection by SAR differential interferometry We will focus on a specific event, the Amatrice earthquake in central Italy on 26 august 2016. First of all, we will consider Sentinel-1 SAR data: a pre-event acquisition, which will be the *master*, taken on 21 august 2016, and a post-event one, which will be the *slave*, taken on 02 September 2016. The earthquake, whose magnitude was 6.2, struck at a shallow depth of 6km; the two considered products are two Sentinel-1A IW SLC images with VH and VV polarization.

Sentinel-1 products are split into 3 subswaths, there is one subswath also for each of the polarization (dual polarization products). If we open IW2VV we can see that there are i and q, because we are treating complex signals which contain also the phase information. Snap is able to automatically compute the intensity from these two bands creating a virtual band.

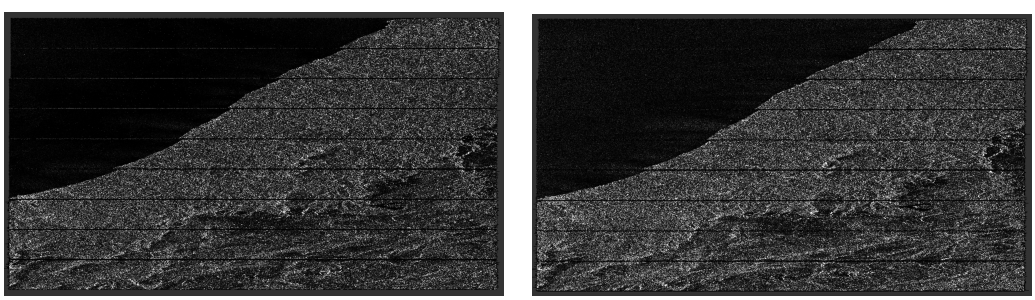

(a) (b)

Figure 1: August (a) and September (b) IW2VV.

There are visible stripes (figure 1): they are called burst; this is due to the kind of operating mode chosen for the S1 SAR instrument, which is called TOPSAR. There are 9 bursts for each subswath. Since the earthquake didn't take all the region, we will work with one polarization, only two subswaths and we will split just for two bursts, which are the ones which cover the area

affected by the earthquake. So, through the Sentinel 1 TOPSAR split, we can choose our area of interest, by setting VV polarization and IW2 subswath; then, we take the burst 5 and 6. The same operation is done for the IW3 subswath taking bursts 6 and 7 (figure 2). Again, we do the same operation for the slave product (figure 3).

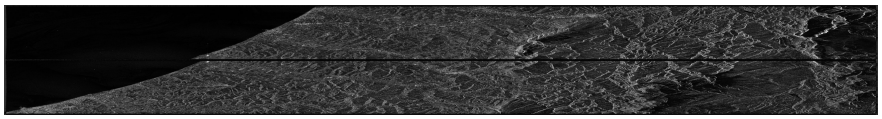

(a)

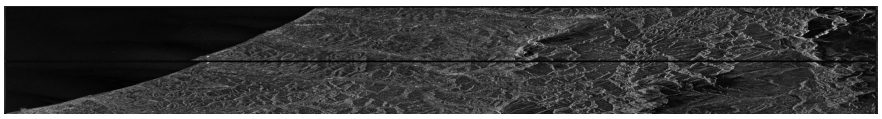

(b)

Figure 2: August (a) and September (b) IW2.

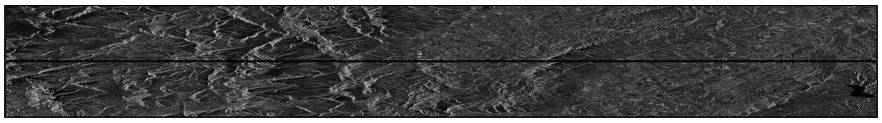

(a)

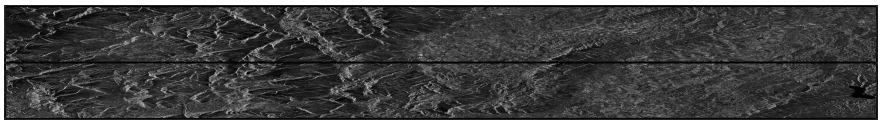

(b)

Figure 3: August (a) and September (b) IW3.

After the split operation, we have all the products of interest split in each subswath: they contain only one subswath and the two bursts we selected. Now, we have to perform the interferometry: the phase of the signal is proportional to the path that the signal took to hit the ground and be back scattered towards the instrument. Exploiting this information, with the second pass that is acquired exactly in the same area we can perform the difference of the phase, which is proportional to the difference of the path that the two signals took. In case there is a deformation, it is possible to derive it from the interferometric phase. Here we have the contributions to the interferometric phase:

$$\Delta\varphi = \Delta\varphi_{flat} + \Delta\varphi_{displacement} + \Delta\varphi_{atmosphere} + \Delta\varphi_{noise} \tag{1}$$

We can see the contribution of the flat earth due to the fact that the earth is not flat, then the term due to the topography (elevation of that particular area) and the one of displacement (deformation on the ground); then we have two unwanted terms: atmosphere and noise, that we can mitigate. The first operation is to register master and slave acquisitions, then subtract the contribution of the flat earth.

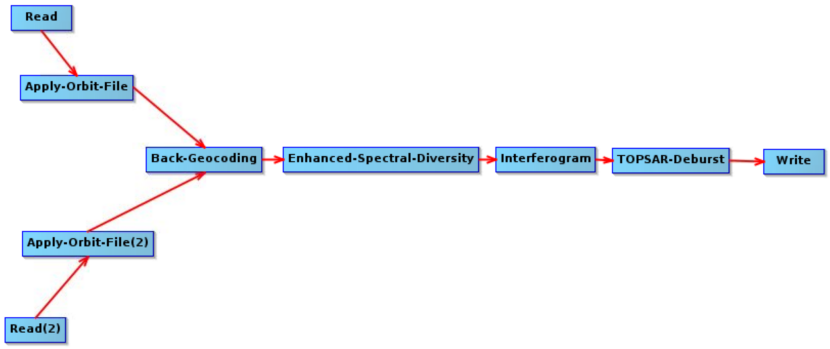

Figure 4: Graph.

By using the GraphBuilder in Snap, we can read master and slave products as a first operation, and then the *Back Geocoding* is the operation needed to register the acquisitions; before computing the interferogram, we add another step, which is *Enhanced Spectral Diversity*, to compensate some issues that we have in the areas that are present between two consecutive bursts. So it is needed to call this operator in those parts of the burst, in order to avoid discontinuity of the phase. In order to perform interferometry and to have a very precise registration of the image we have to use precise orbital information, in *Apply Orbit file*. Then, in the *Back Geocoding* we use the digital elevation model and we select *bicubic interpolation* for the DEM resampling, while *bisinc 21 point interpolation* for the resampling type. We need to put in output also *deramp* and *demodulation phase*, since this is an intermediate step before applying the *Enhanced Spectral Diversity*. Here we can choose the registration window applied between the overlapping areas of two or more bursts, then we can setup also cross-correlation and coherence thresholds, which are used for tuning. The *Interferogram* is the next step: we need to calculate the interferometric phase and subtract the contribution of the flat earth. We keep the default parameters and we put in the output the coherence product, which provides info about the quality of the interferometric phase; since we want it with square pixels, we apply 10 and 3 coherence range and azimuth windows size. The next operation is the *TOPSAR Deburst* to merge consecutive bursts. The final output products are in figure 5, where we can see the interferometric phase and the coherence, which is the cross-correlation coefficient computed between two master and slave acquisitions: it gives us an indication of the quality of our interferogram and how the two acquisitions are similar between each other (the black points represent the less coherent ones, while the white the most coherent ones).

So we have computed the interferometric phase and subtracted the term of the flat earth. Then, we have to merge them and remove the topographic phase (simulated using a digital elevation model) obtaining finally the displacement plus the contribution of atmosphere and noise.

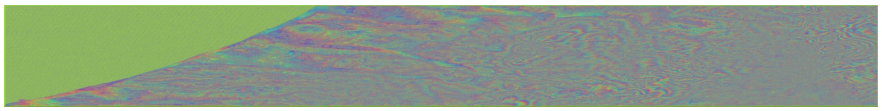

(a) *Interferometric phase*

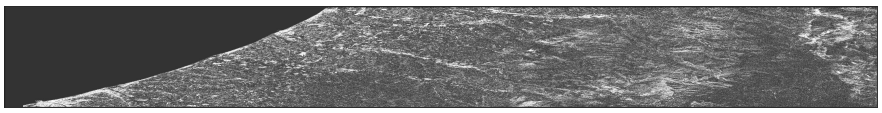

(b) *Coherence*

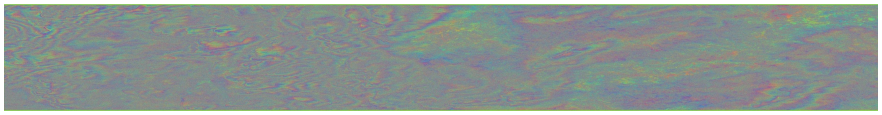

(c) *Interferometric phase*

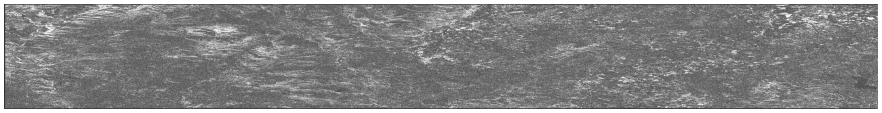

(d) *Coherence*

Figure 5: Interferometric phase and coherence of IW2 (a and b) and of IW3 (c and d).

Now, we have to merge these two outputs through the GraphBuilder (figure 6). Again, we read the two input products previously obtained, then we have the TOPSAR *merge* stage; after this step, we can finally perform the subtraction of the topographic phase with *TopoPhaseRemoval*. Also, it is possible to subset the product to have a particular ROI; after this step, we have a filtering operation done through *GoldsteinPhaseFiltering* and a final operation which is called *Multilook*.

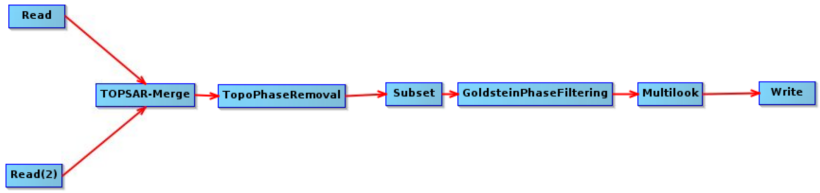

Figure 6: Graph.

The generated image is shown in figure 7 (a). We can see the fringes: each phase cycle, so each fringe, corresponds to a relative displacement of about half of the wavelength:

$$\varphi_d = 2\pi \rightarrow I_{d_{los}} \approx \frac{\lambda}{2} \tag{2}$$

In our case, since the wavelength is 5.6 cm, each fringe corresponds to a displacement of 2.8 cm.

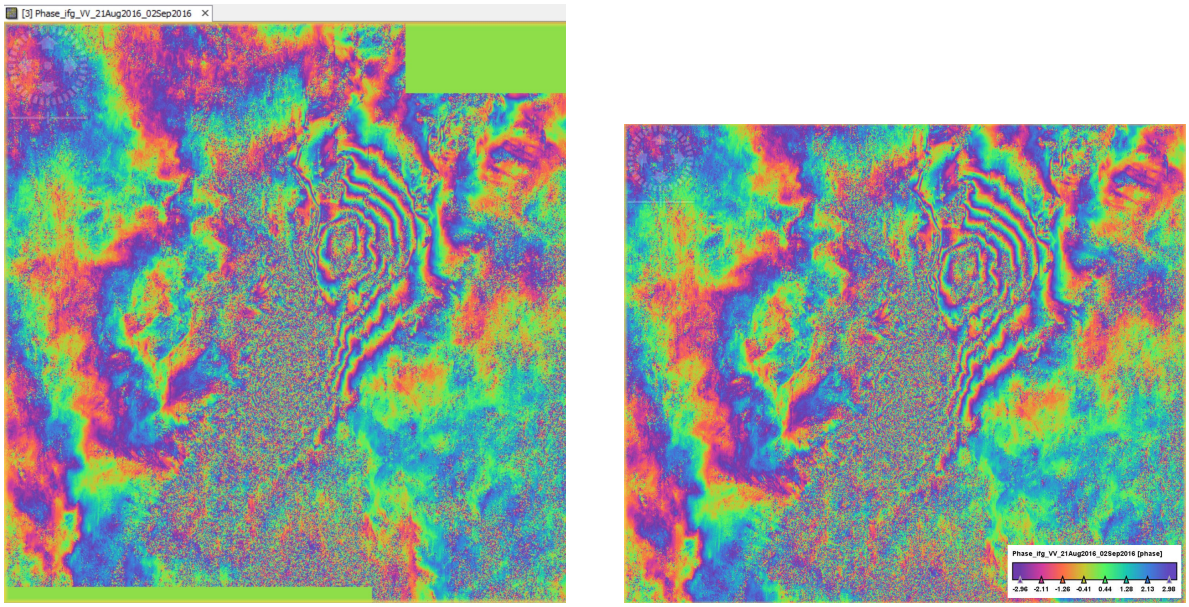

(a) (b)

Figure 7: Phase.

We have about five fringes, so a relative displacement of more than 10 cm. Since we do not have a perfect match of the bursts that were overlapped we have the green part of no data in the image. Hence, we subset again the product (figure 7 (b)).

Now, we have to unwrap such fringes. Once we have only the contribution of the displacement, each fringe corresponds to a deformation of 2.8 cm; there are algorithms that can unwrap the phase cycles, with an operation called *phase unwrapping* (figure 8(a)).

$$\phi = \phi_m + 2\pi k \tag{3}$$

This can be converted into a displacement map. So, by using the Snaphu Export, we choose our interferogram and we import the product through Snaphu Import; then we convert this unwrapped map to a displacement map (figure 8 (b)).

Now, it is possible to have our displacement map terrain corrected: we want to have square pixels that correspond to the ground. Hence we can use the terrain correction operation, putting in input the displacement map with default parameters. After this operation what we obtained can be seen in figure 9 (a).

Here we can see that the red part is the one affected by the deformation, with a negative displacement of more than 13 cm (*subsidence of the terrain*), while the light-blue part has a positive displacement (*uplift of the terrain*). It is also possible to export the map and open it in Google Earth (fig 9 (b)).

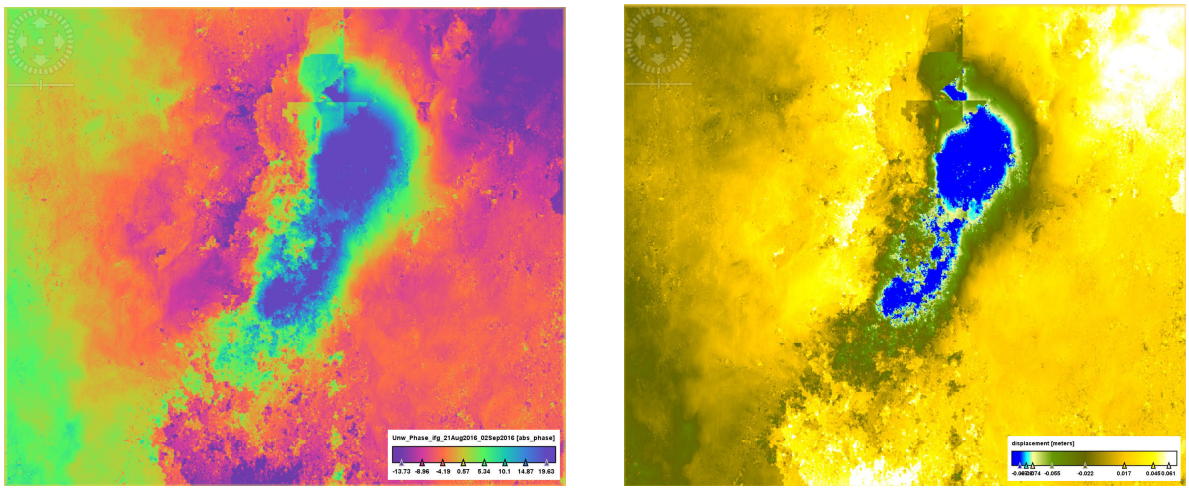

(a) (b)

Figure 8: Unwrapped phase (a) and unwrapped phase converted to a displacement map (b).

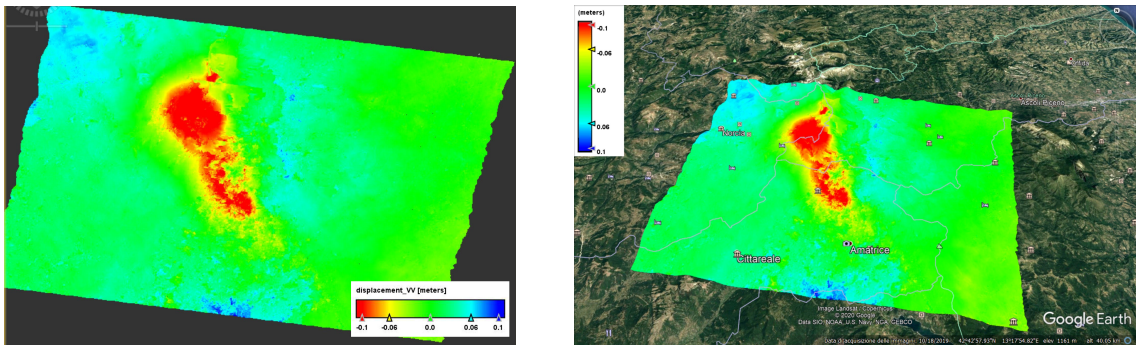

(a) (b)

Figure 9: Displacement map terrain corrected (a) and displacement map in Google Earth (b).

Ship detection by SAR backscattering Another application of S1 SAR data is about ship detection over the Strait of Messina, in Italy. In particular, the selected product is still a product acquired on January 28 of this year in the interferometry wave mode, but it is already ground range detected (namely it does not contain also the phase information as before). So, first of all, we can look at the bands contained in the product: amplitude band and virtual band intensity. The first thing to do is to perform a spatial subset in order to focus on the region of interest (the Strait of Messina, figure 10 (b)).

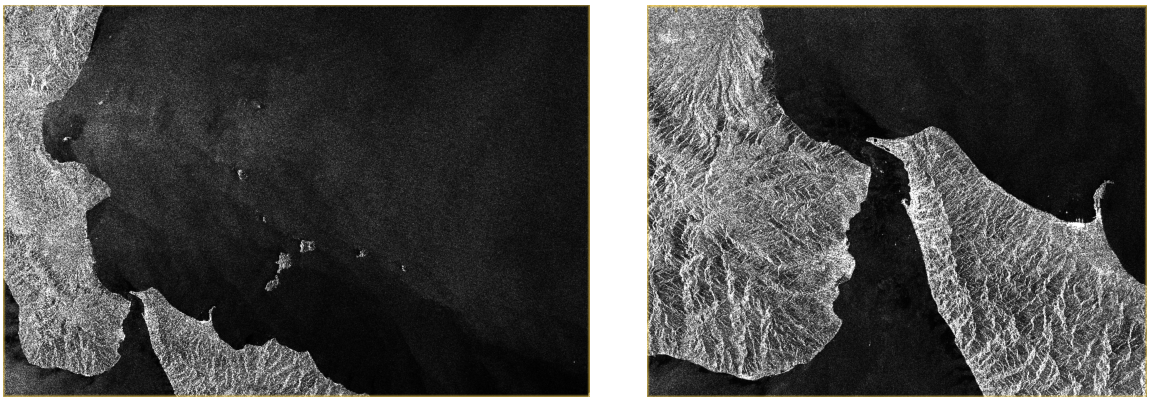

(a) *Intensity VV* (b) *Intensity VV subset*

Figure 10: Intensity VV over the Strait of Messina.

After that, it is needed to apply the precise orbit file on this product and then to perform the *Ocean object detection*. Since the objective is to work over the sea, we masked out the land with the help of the SRTM digital elevation model; we also extended the shortline to 50 pixels in order to avoid false alarms over the coast. The next operation is the calibration: here we need to pass from the amplitude of our signal to a product related to the actual backscatter coefficient of the target surface, and in our case, we can put in the output the so-called *sigma0 band*. The next step is the core of the algorithm, which is the *adaptive thresholding*: in fact, the object detection is performed in an adaptive way by the above mentioned operator. It is a frequently used method for target detection in SAR imagery: the underlying assumption is that targets appear bright on dark background. The algorithm is applied in a moving window. For each pixel under test (central pixel) a new threshold value is calculated based on the statistical characteristics of its local background: if the pixel value is above the threshold the pixel is classified as the target pixel.

For each pixel there are three windows: the *target window*, with a chosen size of 30 meters (which is the length of the smallest target to detect), a *guard window*, 500 meters, that corresponds to the maximum extent of the target that we could detect, then there is a *moving window* (namely the background pixels), with the size of 800 meters, larger than the guard window size to ensure accurate calculation of the background statistics.

First, the detector design parameter t is computed. Then, the background mean μ_b and the standard deviation σ_b are computed, using the pixels in the background ring; then, the mean value of the target window μ_t is also computed; now, if the following condition is satisfied, the center pixel is detected as part of an object, otherwise not:

$$\mu_t > \mu_b + \sigma_{b^*} t \tag{4}$$

Subsequently, the windows are moved by one pixel to detect the next one. We tune the parameters and we set the probability of false alarm to 12.5. The next step is object discrimination: it will scan all the pixels that were selected by the adaptive thresholding operation and it will detect the target that corresponds to the chosen parameters, namely it will filter out false targets based on minimum and maximum size limits (which in our case are respectively 30 and 600 meters). In the end, what we obtain is shown in figure 11.

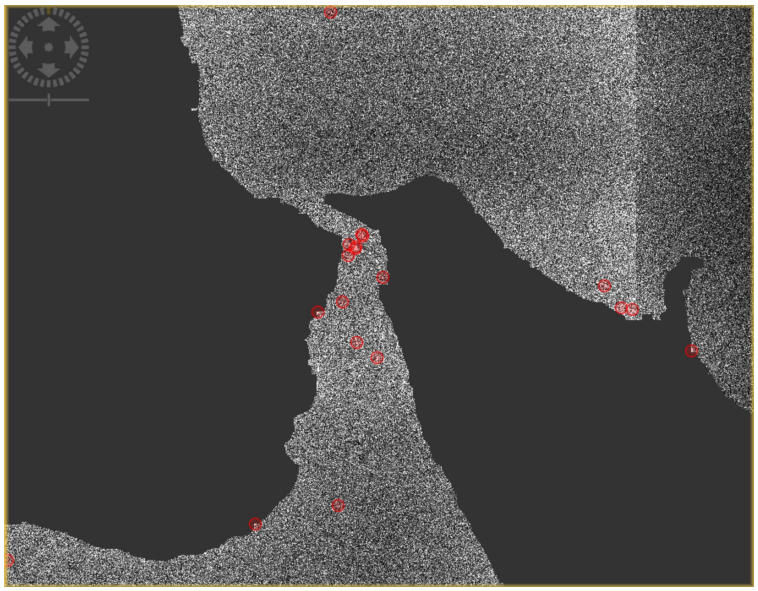

Figure 11: Ship detection sigma0 band.

The red circles in the image (figure 12), highlighted with the help of the colour manipulation tool, correspond to the detected ships in the sea over the Strait of Messina.

(a) *Sigma0 VV*

ShipDetections	geometry	Detected_x	Detected_y	Detected_lat	Detected_lon	Detected_width	Detected_length	style_css
target_000	POINT (326...	3264	109	38.438	15.693	120	260	fill: #ff0000;...
target_001	POINT (357...	3576	2336	38.243	15.608	160	200	fill: #ff0000;...
target_002	POINT (357...	3578	2352	38.241	15.608	40	50	fill: #ff0000;...
target_003	POINT (344...	3445	2431	38.232	15.621	90	100	fill: #ff0000;...
target_004	POINT (350...	3501	2472	38.229	15.614	280	280	fill: #ff0000;...
target_005	POINT (351...	3511	2460	38.231	15.613	90	40	fill: #ff0000;...
target_006	POINT (343...	3439	2546	38.222	15.619	140	140	fill: #ff0000;...
target_007	POINT (627...	6274	3086	38.219	15.289	110	250	fill: #ff0000;...
target_008	POINT (600...	6001	2844	38.236	15.325	250	230	fill: #ff0000;...
target_009	POINT (617...	6171	3069	38.219	15.301	150	180	fill: #ff0000;...
target_010	POINT (337...	3375	3007	38.179	15.616	100	200	fill: #ff0000;...
target_011	POINT (313...	3131	3111	38.166	15.641	180	220	fill: #ff0000;...
target_012	POINT (378...	3781	2765	38.208	15.576	130	80	fill: #ff0000;...
target_013	POINT (686...	6869	3496	38.192	15.214	50	120	fill: #ff0000;...
target_014	POINT (352...	3524	3418	38.145	15.591	160	140	fill: #ff0000;...
target_015	POINT (372...	3721	3567	38.134	15.565	120	280	fill: #ff0000;...
target_016	POINT (333...	3333	5049	37.994	15.578	120	280	fill: #ff0000;...
target_017	POINT (250...	2506	5231	37.964	15.667	150	200	fill: #ff0000;...
target_018	POINT (30 5...	30	5597	37.89	15.936	70	70	fill: #ff0000;...

(b)

Figure 12: Ship detection data.

Flood detection by SAR backscattering Finally, the third application is flood detection. We will do this by studying a flood that occurred in Mozambique, in Africa, on the 14 of March 2019. In particular, two SAR images will be used: the first one is a pre-event acquisition (acquired on the 13 of March) and the second one is a post-event acquisition (acquired on the 19 of March).

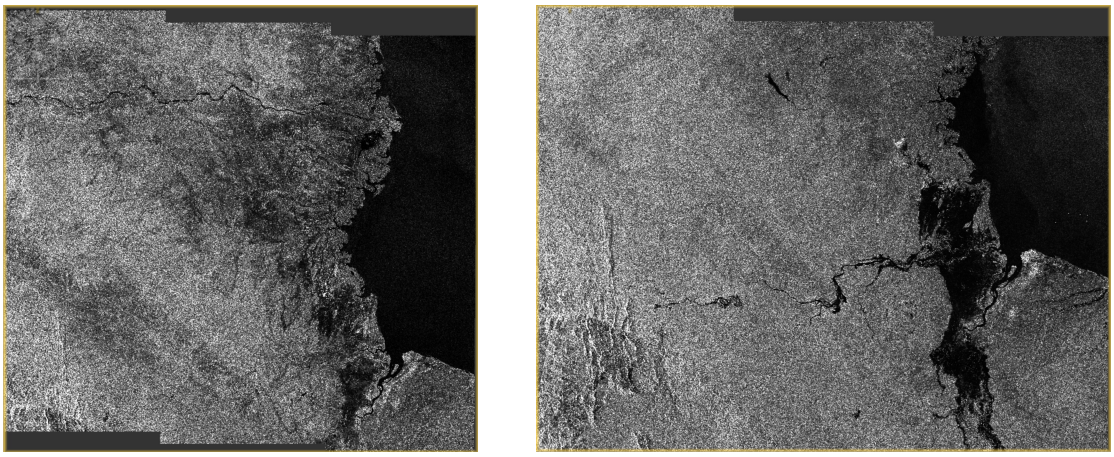

(a) *Pre-event intensity* (b) *Post-event intensity*

Figure 13: Pre-event and post-event acquisition in the flooded area in Mozambique.

The dark part in the second image (13 (b)) is, most likely, the flood. This darker part corresponds to a very low backscatter because, in presence of water, it is possible to have a specular reflection of the transmitted signal from the SAR instrument. A very small part of this signal is backscattered to the sensor: that's why the coefficient is very low, which will corresponds to a very dark part in the image. In the pre-event acquisition it is easy to see that we don't have the dark area (this means that the flood has not occurred yet).

Through the GraphBuilder tool, the following operations have been performed:

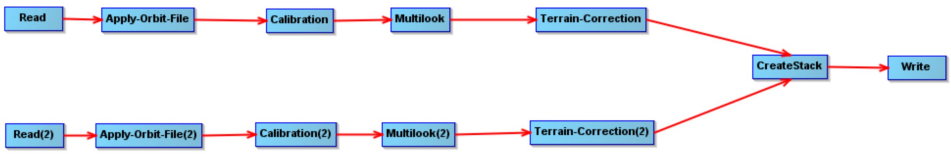

Figure 14: Graph.

As usual, we take the two input images, then we apply the *precise orbit file* for both of them; the next operation is to calibrate the product with the VV polarization, choosing for the output the Sigma0 band. Then, the *multilook* operation is also performed: we want to increase the number of range and azimuth looks to 9 and that will corresponds to ground range square pixels of 90 m (since that corresponds to the digital elevation model resolution that we will use). Finally, we also perform the *geometric terrain correction* and, at the end, we stack the two processed images in one

single product by using the *CreateStack* operation: we choose product geolocation for the initial offset method. The output of the graph is shown in figure 15.

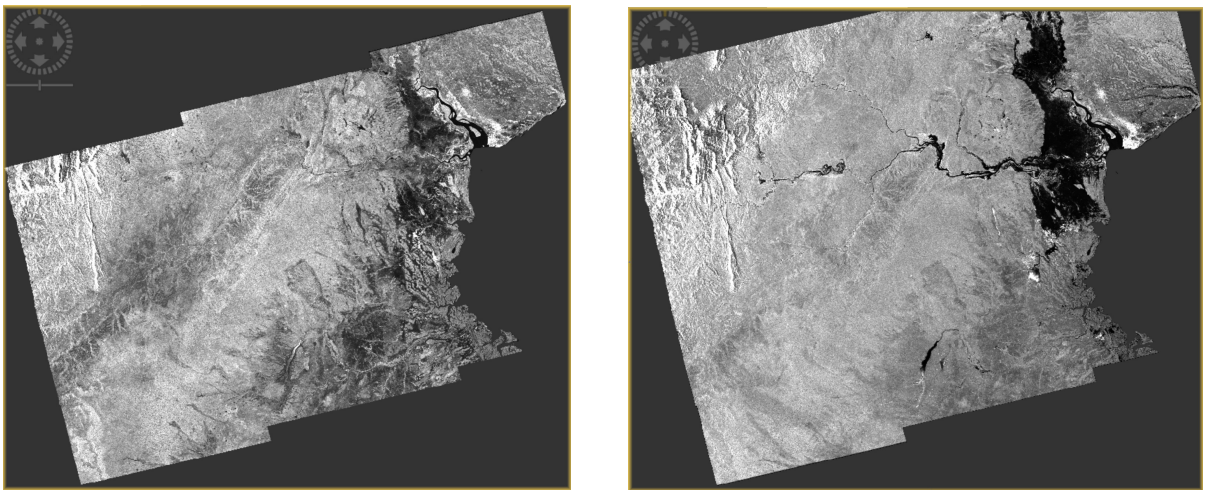

(a) *Pre-event intensity* (b) *Post-event intensity*

Figure 15: Processed pre-event and post-event acquisition in the flooded area in Mozambique.

Then, it is possible to go from a linear scale to a logarithmic one, by converting both bands from linear to decibel: this will generate a new virtual band.

Now, it is possible to perform a change detection between the master pre-event acquisition and the slave post-event one. In the first, we are supposed to not see the effect of the flood, which is instead visible in the post-event acquisition; in presence of flood (water) the backscatter of the SAR acquisition is significantly reduced because it is increased the factor of specular reflection of the signal in the surface. By exploiting this behaviour of our target in presence of water, we can perform a change detection between pre and post-event acquisition by combining the two bands and checking the difference. A qualitative method consists in creating an RGB composite by combining the values of the two bands. In particular, we will set the red channel equal to the backscatter of the pre-event image only if the difference in absolute value w.r.t. the other product is higher than 3 dB; the same condition applies for the green and blue channels: if the condition is satisfied, then they will be set equal to the master. In this way, we are trying to discard all the possible minor differences between the two acquisitions, and just considering the one with a higher entity. Since the slave image is put on red channel, the case we see red pixels in the final output product will correspond to the part of the image where the backscatter of the post-event (slave) acquisition is higher than the pre-event (master) acquisition. This should not be the case of the flood condition (which implies the presence of water which decreases the backscatter). Instead, since the master acquisition is put on green and blue channels, if we see pixels in cyan color in the final output image, they correspond to pixels where the pre-event backscatter is significantly higher than the post-event backscatter: this should correspond most likely to the condition of presence of water, namely the flood.

Those conditions will be put into Snap in the form of expressions.

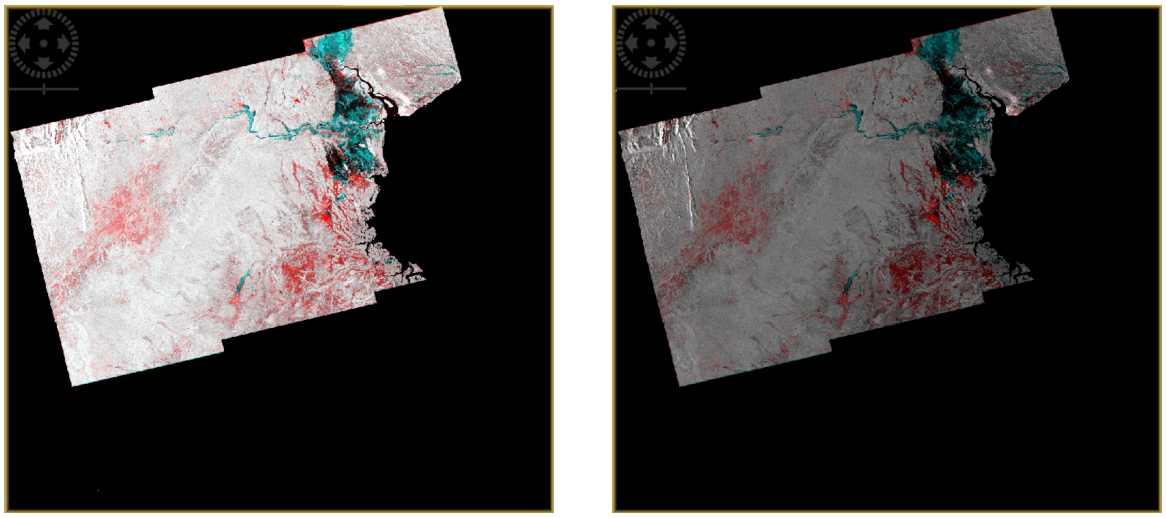

(a) *Virtual RGB* (b) *Virtual RGB with uniform scale* [−15, 0]

Figure 16: RGB combined bands.

After a color manipulation, we can see that the flooded area is in cyan, where the backscatter of the post-event acquisition is lower than the one of the pre-event acquisition, while the red part corresponds to cases where the backscatter of the post-event acquisition is higher than the other, which are cases not related to our observed flood. Instead, the grey, white and black pixels correspond to the part of the image where the backscatter of both master and slave remains the same between the two acquisitions (in fact we put the threshold of 3 dB, so in case of very small differences we set that value to the average of them: we are forcing them to be grey, in some cases). The black parts correspond to the case in which the backscatter is low in both of them, while the white pixels could be urban areas where the backscatter of both acquisitions is instead high for both of them.

Conclusions The main subjects of this work were the SAR differential interferometry and backscattering, in particular their application for earthquake, ship and flood detection. In fact, Sentinel-1 SAR data in different times of the year and in different areas were taken into account. First of all, we focused on the Amatrice earthquake in central Italy by performing the DInSAR processing steps with the help of the GraphBuilder tool in Snap: starting from a master and a slave (pre and post-event) input data, we arrived at a final product, namely a displacement map with terrain correction, with visible subsidence and uplift of the terrain, showing the presence of a deformation caused by an earthquake. Then, a ship detection over the Strait of Messina was performed, by means of SAR backscattering; this was done by first subsetting around a ROI, then the orbit precising, land-sea masking and calibration steps were performed and finally the adaptive thresholding algorithm was applied, for the object detection purpose. Finally, the last application was related to flood detection in Mozambique, through SAR backscattering. As we showed during the discussion, after the main DInSAR processing steps, we were able to perform a change detection between pre-event and post-event acquisitions, noting that there was a reduction of the backscatter of the SAR acquisition in presence of water: hence, a qualitative change detection was possible by

RGB band combination.

References

[1] Alessandro Ferretti, Andrea Monti-Guarnieri, Claudio Prati and Fabio Rocca, "InSAR Principles: Guidelines for SAR Interferometry Processing and Interpretation", ESA 2007

[2] "Geoscience and Remote Sensing", IEEE GRSS 2012

[3] Alberto Moreira, Pau Prats-Iraola, Marwan Younis, Gerhard Krieger, Irena Hajnsek and Konstantinos P. Papathanassiou, "A Tutorial on Synthetic Aperture Radar", IEEE Geoscience and remote sensing magazine March 2013